RESEARCH ARTICLE

MICROSCOPY RESEARCH&TECHNIQUE WILEY

3D-quantum interferometer using silicon microring-embedded gold grating circuit

Arumona Edward Arumona[1,2,3] | Iraj Sandegh Amiri[1] | Suphanchai Punthawanunt[4] |
Kanad Ray[5] | Ghanshyam Singh[6] | Gaurav Kumar Bharti[7] | Preecha Yupapin[1,2]

[1]Computational Optics Research Group, Advanced Institute of Materials Science, Ton Duc Thang University, District 7, Ho Chi Minh City, Vietnam

[2]Faculty of Applied Sciences, Ton Duc Thang University, District 7, Ho Chi Minh City, Vietnam

[3]Division of Computational Physics, Institute for Computational Science, Ton Duc Thang University, Ho Chi Minh City, Vietnam

[4]Faculty of Science and Technology, Kasem Bundit University, Bangkok, Thailand

[5]Amity School of Applied Sciences, Amity University Rajasthan, Jaipur, Rajasthan, India

[6]Department of ECE, Malaviya National Institute of Technology Jaipur (MNIT), Jaipur, Rajasthan, India

[7]Department of Electronics and Communication Engineering, Techno Engineering College Banipur, West Bengal, India

Correspondence
Preecha Yupapin, Faculty of Applied Sciences, Ton Duc Thang University, District 7, Ho Chi Minh City, Vietnam.
Email: preecha.yupapin@tdtu.edu.vn

Review Editor: Alberto Diaspro

Abstract

A 3D (three-dimensional) quantum interferometer consisting of a silicon microring circuit proposed. The interferometer based on the electron spin cloud projections generated by microring-embedded gold grating. The electron cloud oscillations result from the excitation of the gold grating at the center of the silicon microring by the dark soliton pulse of 1.50 μm center wavelength. The electron cloud spin-down, spin-up automatically formed in the two axes (x, y, respectively) and propagated along the z-axis. In this proposal, the sensing mechanism of the circuit is manipulated by varying the reflector gold lengths of the sensing arm. The electron cloud spin coupled and changed by changing the gold lengths. The sensitivity measurement of the 3D quantum interferometer for three gold layer lengths of 100 nm, 500 nm, and 1,000 nm is (47.62 nm fs^{-1}, ±0.4762 fs^{-1}, ±0.01 nm^{-1}), (238.10 nm fs^{-1}, ±0.4762 fs^{-1}, ±0.002 nm^{-1}), (476.20 nm fs^{-1}, ±0.4762 fs^{-1}, ±0.001 nm^{-1}), respectively. The used circuit parameters are the real ones that can be fabricated by the currently available technology. Moreover, the silicon micro ring circuit acts as a plasmonic antenna, which can apply for wireless quantum communication. The electron cloud spin projection space–time control can apply for quantum cellular automata.

KEYWORDS
3D interferometer, optical interferometer, plasmonic interferometer, quantum interferometer

1 | INTRODUCTION

The principle of the interferometer is that lights of two or more sources merged to form interference (Yang & Zhang, 2018), where the interference patterns have useful information for various applications. It is a useful instrument for small change measurements. Interferometers group into classical and quantum types. Principally, the quantum interferometer can be classified based on their mode of operation. Quantum interferometer requires the input entangled source, where various works of quantum interferometers reported. Quantum interferometer like Hong-Ou-Mandel interferometer uses entangled photons to form the interference (Chen, Fink, Steinlechner, Torres, & Ursin, 2019; Kim, Lee, Kwon, & Moon, 2017; Spagnolo et al., 2012; Zhang, Guo, Gao, Gao, & Yang, 2017). Quantum interferometer like matter-wave interferometer is based on entangled electron interference (Amit et al., 2019; Filip et al., 2019; Nadine et al., 2014; Pooch, Seidling, Layer, Rembold, & Stibor, 2017). Many types of interferometers (Bass, Eric, David, & William, 1994) like the plasmonic interferometer based on the excitation of electrons generated by the surface plasmon waves. The formation of surface plasmon polariton (SPP) is designed in different forms, where usually one of the material components of every design is either gold or silver. Khajemiri et al. investigated biochemical sensing both experimentally and theoretically using a novel plasmonic interferometer (Khajemiri, Lee, Hamidi, & Kim, 2019). Their plasmonic interferometer has a rectangular

shape, and one of the material components is gold. Li et al. used a plasmonic optical interferometer at nanoscale (Li, Feng, & Pacifici, 2016), where the optical interference of incoherent light sources is employed. They have shown that the plasmonic interferometer using a thin silver film sensor can work in various environmental conditions. Zulicke and Signal developed a Rashba interferometer that is electron spin-dependent and is used to study the relationship between quantum interference and spin precession of electrons (Zulicke & Signal, 2007). Nandy et al. studied the magneto-transport and electron states in a fractal AB interferometer (Aharonov-Bohm) (Nandy, Biplab, & Chakrabarti, 2014), where the renormalization group of real space and tight-binding model used. In this work, a 3D-quantum interferometer is based on electron cloud generated by silicon microring-embedded gold grating, which employed for sensing applications. The interferometer has the form of the panda-ring (Tamee, Srinuanjan, Mitatha, & Yupapin, 2011), which consists of a silicon microring with gold gratings embedded at the center of the silicon microring (Nagarajan, Van Erve, & Gerini, 2020), two linear waveguides, and the gold layer are located at the tips of the linear waveguides. The manipulation used two simulation programs based on the device parameters. First, the Optiwave FDTD program is employed for the graphical investigation. The formation of the whispering gallery mode (WGM) (Foreman, Swaim, & Vollmer, 2015; Punthawanunt et al., 2018; Trong & Chang, 2017) by the soliton input formed by electron cloud trapping, and its loss-less transportation is required and we achieved it. The obtained optimum parameters are extracted from the simulation results. Second, the Matlab program is employed using the extracted parameters from the Optiwave FDTD program, and the quantum interference is simulated leading to other results.

2 | THEORETICAL BACKGROUND

The schematic and fabrication structure of the 3D quantum interferometer shown in Figure 1, which has the form of panda ring. There are two linear waveguides, silicon microring, two nanorings at the side of the microring, gold gratings embedded at the center of the microring, and gold layer at the tips of the linear waveguides. The interference fringe of the interferometer can be described by Equation (1) as (Szuatakowski & Palka, 2005):

$$I(\Delta I) = I_0\left(k_{12}^2 k_{22}^2 r_A^2 + k_{13}^2 k_{32}^2 r_B^2\right)\left[1 + V(\Delta I)\cos\left(\frac{4\pi}{\lambda_0}N[D - \Delta I(1 - p_e)]\right)\right] \quad (1)$$

where I, V, D, I_0, N, λ_0, k_{ij}, r_A, R_B, and p_e are output irradiance, interferometer contrast, arm length difference, input source irradiance, waveguide effective refractive index, light source wavelength, amplitude coefficients, waveguide end reflection coefficients, and waveguide elastic coefficient. $V(\Delta I)$ is given in an Equation (2) as:
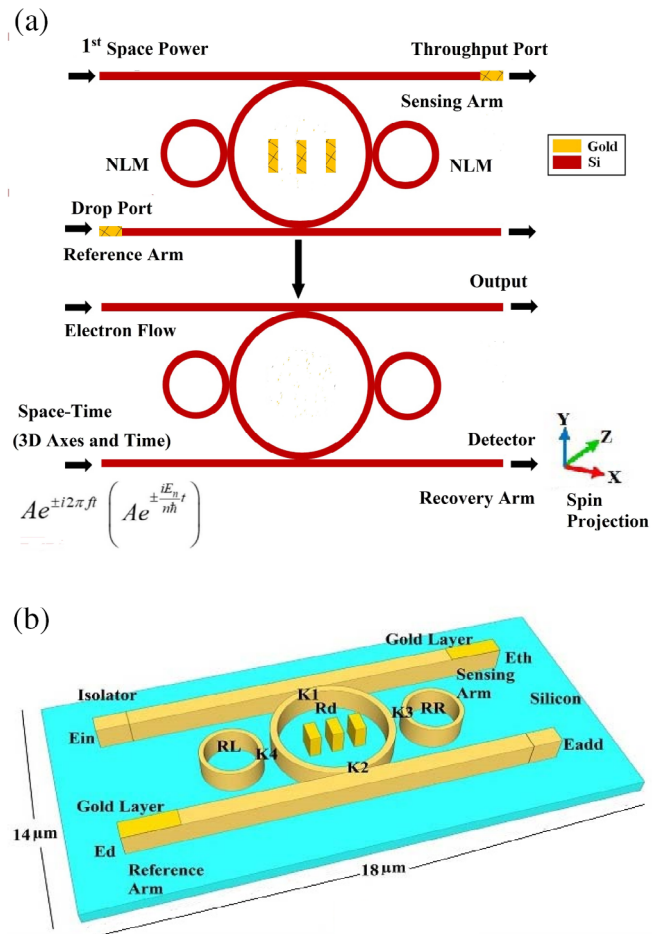

FIGURE 1 3D quantum interferometer system, where (a) a schematic diagram; NLM is the nonlinear phase modulator, the first space input source is a soliton pulse. Gold gratings are at the center ring with the gold layer at the tips of the sensing and reference arms, (b) a fabrication structure: where the input, throughput, add port, and drop ports are E_{in}, E_{th}, E_{add}, and E_d, respectively. Rd: central ring radius, RR and RL: side ring radii, K1- K4: coupling constants. The isolator is applied to protect the feedback [Color figure can be viewed at wileyonlinelibrary.com]

$$V(\Delta I) = \frac{k_{12}k_{22}r_A k_{13}k_{32}r_B}{k_{12}^2 k_{22}^2 r_A^2 k_{13}^2 k_{32}^2 r_B^2}\left(\sum_{q=1}^{p} H_q\right)^{-1}$$

$$\times \exp\left[-\left(\frac{\pi N}{\sqrt{\ln 2}}\frac{\Delta\lambda}{\lambda_0^2}[D - \Delta I(1 - p_e)]\right)^2\right]$$

$$\times \sqrt{\left(\sum_{q=1}^{p} H_q\cos(A)\right)^2 + \left(\sum_{q=1}^{p} H_q\sin(A)\right)^2} \quad (2)$$

where $A = \left(\frac{4\pi}{\lambda_0^2}\Delta\lambda_1(q-1)N[D - \Delta I(1 - p_e)]\right)$, $\Delta\lambda$, $\Delta\lambda_1$, and H_q are the spectral width, mode spacing, and mode amplitude.

The first space input source is the dark soliton pulse with the wavelength λ_1 as given in an Equation (3) (Agrawal, 2011), and the multiplexed space–time source applied into the system, which is given in an Equation (4). When the soliton pulse excites the gold grating at the center of the microring, which results in electron cloud oscillations which process

the electron spin down $|\downarrow\rangle(|1\rangle)$ with spin matrix $\frac{\hbar}{2}\begin{vmatrix} 0 & 1 \\ 1 & 0 \end{vmatrix}$, and electron spin up $|\uparrow\rangle(|0\rangle)$ with the spin matrix $\frac{\hbar}{2}\begin{vmatrix} 1 & 0 \\ 0 & -1 \end{vmatrix}$ (Russ & Burkard, 2017). The superposition can be any of the two states of the electron spin $|\Psi\rangle = \alpha|0\rangle + \beta|1\rangle$ with $|\alpha|^2 + |\beta|^2 = 1$. The spin number is $\pm\frac{\hbar}{2}$, $\hbar$ is the reduced Planck's constant. The behavior of the electrons is described by the Drude model as given in the Equation (5) (Prince, 2018; Tunsiri, Thammawongsa, Threepak, Mitatha, & Yupapin, 2019).

$$E_{in} = \bar{D}.Tanh\left(\frac{T}{T_0}\right)exp\left(\frac{z}{2L_D}\right) \quad (3)$$

where $\bar{D}$ is the amplitude, z is the propagation distance, T is the propagation time of the soliton pulse, the length dispersion $L_D = \frac{T_0^2}{\beta}$, where T_0 is the initial propagation time, β is the linear and nonlinear propagation constant .

The multiplexed space–time source applied to the system, which is expressed by

$$E_{add} = B.e^{\pm i\omega t} \quad (4)$$

where $\omega = 2\pi f$, $f = \frac{c}{\lambda_1}$, ω, f, c are the angular frequency, linear frequency, and speed of light in vacuum, respectively. B and t are the amplitude and time, respectively. The $\pm$ signs of the exponent term used for the full-time slot axis; the control time is given by $e^{\pm i\omega t}$ and $t = 0$ for the time domain.

$$\epsilon(\omega) = 1 - \frac{ne^2}{\epsilon_0 m\omega^2} \quad (5)$$

The relative permittivity defined by ϵ_o, electron charge defined by e, mass defined by m, and the electron density defined by n and angular frequency defined by ω_p.

At resonance, the angular frequency becomes the plasma frequency (ω_p), which is written in an Equation (6) as:

$$\omega_p = \left[\frac{ne^2}{\epsilon_0 m}\right]^{-\frac{1}{2}} \quad (6)$$

From Equation (6), the electron density $n = \frac{\omega_p^2}{e^2}\epsilon_0 m$. The plasmonic wave oscillation is a consequence of electron density in an electric field. To obtain the exponent decay and TM-polarization of the electric field, Maxwell equations are employed. The Bragg and resonant wavelengths are related by $\lambda_B = 2n_e\Lambda$, where the Bragg wavelength is λ_B. The effective refractive index is n_e, which is also the refractive index of the gold gratings inside the waveguide and grating period is Λ. Kerr effect exists through the structure, and it can be included in the $n = n_0 + n_2 I = n_0 + n_2 P/A_{eff}$ equation. n is the refractive index, n_0 is the linear refractive index, n_2 is the nonlinear refractive index, I is the optical intensity, P is the optical power, and A_{eff} is the effective core area. The effective core area is the area of light coupled effectively into the waveguide, which is fixed in this work.

The two nanorings at the sides of the silicon microring act as phase modulators which control the whispering gallery mode at resonance

and through the throughput and drop ports the normalized intensities are obtained. The output fields are described by Equations (7) and (8) (Pornsuwancharoen et al., 2018; Prateep, Surasak, & Yupapin, 2016; Yupapin, Pornsuwanchroen, & Chaiyasoonthorn, 2008).

$$E_{th} = m_2 E_{in} + m_3 E_{add} \quad (7)$$

$$E_{drop} = m_5 E_{add} + m_6 E_{in} \quad (8)$$

where m_i and the related terms are the constants and found in the given references. Throughput port (E_{th}), drop port (E_{drop}), add port (E_{add}), and input port (E_{in}), respectively.

The normalized intensities of the system output written as:

$$\frac{I_{th}}{I_{in}} = \left[\frac{E_{th}}{E_{in}}\right]^2 \quad (9)$$

$$\frac{I_{drop}}{I_{in}} = \left[\frac{E_{drop}}{E_{in}}\right]^2 \quad (10)$$

From Equations (9) and (10), the first space function is a soliton input via an input port. Two side rings control the successive filtering of the transmission circuit. The nonlinear effect coupled with the center ring, which affected the resonant transmission. The spin projection applied at the resonance condition at the drop port, whereas the throughput formed the reference port.

3 | RESULTS AND DISCUSSION

The Optiwave FDTD program employed as a first step in the simulation, from which the WGM and electron cloud obtained. The input light from the dark soliton fed into the system as shown in Figure 1b. It is an entangled source with a center wavelength of 1.50 μm, which is input via the input port into the circuit. The entangle source is suitable for space–time control. The oscillation of polariton dipoles occurs when the electrons excited by the plasmonics waves through the gold grating at the center ring, where the Bragg wavelength formed, which is a result of the gold grating shifting the center wavelength. The whispering gallery mode formation is a result of the coupling of light inside the microring with two side rings. It coupled into the gold grating at the center of the microring and with a particular wavelength at resonance, where the oscillated electron cloud trapped inside the microring. The output signals obtained via device output ports are the throughput and drop ports. In the 32-bit version (OptiFDTD, 2019), 12.0 of the Optiwave FDTD program employed for the simulation of the system has a grid size of 0.05 with the mesh cell size of 274, 49, and 314 for the three axes (x, y, z, respectively). The type of boundary condition employed is the APML, which is the anisotropic perfect matched layer. The APML has a layer of 15, real tensor of 1.0, and 1.0 theoretical reflection coefficient. For the confirmation of the resonant results, the simulation runs for 20,000 round trips. The formation of the whispering gallery mode using suitable parameters in Table 1 is shown in Figure 2. The parameters from the results of the

Parameters	Symbols	Values	Units
Input power (dark soliton)	P	20	mW
Length of silicon linear waveguide	L	15.0	μm
Silicon center ring radius	Rd	3.0	μm
Left nanoring radius	RL	1.0	μm
Right nanoring radius	RR	1.0	μm
Gold dielectric constant (Pornsuwancharoen et al., 2017)	ϵ_o	6.9	
Gold permittivity (Pornsuwancharoen et al., 2017)	ϵ	10.0	
Gold layer length	La	100, 500, 1,000	nm
Width of Au grating	W_{AU}	0.4	μm
Thickness of Au grating	d	0.2	μm
Length of Au grating	L_{AU}	1.6	μm
Refractive index of Au (Pornsuwancharoen et al., 2017)	n	1.80	
Insertion loss	γ	0.5	
Mode amplitude	H_q	1.0	
Coupling coefficient	K	0.7–1.0	
Amplitude coefficient	k_{ij}	0.01	
Refractive index Si (Prabhu, Tsay, Han, & Van, 2010)	n_{Si}	3.42	
Reflection coefficient	r_A, r_B	0.5	
Elastic coefficient	p_e	0.22	
Si nonlinear refractive index (Prabhu et al., 2010)	n_2	1.3×10^{-13}	$m^2\,W^{-1}$
Input light wavelength	λ_1	1.50	μm
Waveguide core effective area (Pornsuwancharoen et al., 2017)	A_{eff}	0.30	μm^2
Waveguide loss	α	0.50	$dB\,(cm)^{-1}$
Plasma frequency (Blaber, Arnold, & Ford, 2009)	ω_p	1.2990×10^{16}	$rad\,sec^{-1}$
Electron mass	m	9.11×10^{-31}	kg
Electron charge	e	1.6×10^{-19}	Coulomb
Permittivity of free space	ϵ_o	8.85×10^{-12}	$F\,m^{-1}$
Reduced Planck's constant	$\hbar$	1.00	ARU

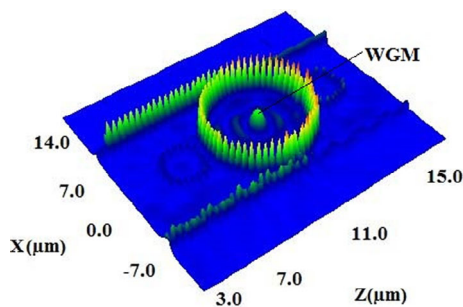**TABLE 1** The selected parameters used in simulation

FIGURE 2 Plot of the Optiwave results: with the formation of the whispering gallery mode (WGM) at the center of the main ring of the microring circuit, where Rd = 3.0 μm, RR = 1.0 μm, RL = 1.0 μm, each K = 0.50, Input power = 20 mW, with the center wavelength of 1.50 μm, and other parameters given in Table 1 [Color figure can be viewed at wileyonlinelibrary.com]

Optiwave FDTD simulation are extracted and used in the MATLAB program. Following the schematic diagram is as shown in Figure 1a, the first space input source is the dark soliton given in an Equation (3). It fed into the system described by the Equations (7)–(8). The dark soliton excites the gold grating, which leads to electron cloud oscillation and forming the electron density $[n = \frac{\omega_p^2}{e^2}\epsilon_0 m]$. The trapped electrons transport through the throughput port and drop port, where the sensing interferometer formed by the interference of the reflected of the sensing and reference arms. The change in electron cloud at the center ring induced the change in the optical path difference and interferometer output fringes, which can be balanced (recovery) by moving the recovery arm.

From Figure 1, the sensing interferometer and recovery interferometer connected fusion splice. In this article, the changes in the electron cloud spin manipulated by the changes in gold (reflector)

lengths. The space–time control applied via the add port, where the space input source multiplexed with time to form the space–time input source as given in Equation (4). The spin to the x-axis, the y-axis is the spin-down $|1\rangle$, spin-up $|0\rangle$, respectively, propagates along the z-axis with the effect of the quantum interference, which described by Equation (1) and detected at the recovery arm. The gold layer lengths at the sensing arm varied, whereas the gold layer length at the reference arm fixed. The changes in the gold layer length at the sensing arm affects the final output at the recovery arm. By using the Equations (9) and (10), the final output of the recovery arm is balanced, where the change in the quantum interferometer is obtained. In Figure 3, the generation of the electron spins with the change in gold layer length shown. Figure 3a–c is the electron spin down (spin-x) and spin up (spin-y) propagating along the z-axis (spin-z) for the gold layer length of 500 nm and also for 1,000 nm as shown in Figure 3d–f. The projection of the electron

spins into the plane using the gold layer length of 500 nm is shown in Figure 4a–c and also for 1,000 nm shown in Figure 4d–f. The 3D quantum interferometer manipulation results are shown in Figure 5a–c, where the linear relationships of the sensing sensitivities achieved. The length of the plot increased as the gold layer length increased. The sensitivity graph is shown in Figure 6, which is the combination of the three different plots in Figure 5. The slopes of the sensitivity graph for 100 nm are 47.62 nm fs^{-1} in the x–y direction, ± 0.4762 fs^{-1}, ± 0.01 nm^{-1} in the x–z and y–z directions, respectively. For 500 nm, the slopes are 238.10 nm fs^{-1} in the x–y direction, ± 0.4762 fs^{-1}, ± 0.002 nm^{-1} in the x–z and y–z directions, respectively. Finally, for 1,000 nm, the slopes are 476.20 nm fs^{-1} in the x–y direction, ± 0.4762 fs^{-1}, ± 0.001 nm^{-1} in the x–z and y–z directions, respectively. In Figures 5 and 6, the blue color represents the spin up in the y-axis, red color represents the spin down in the x-axis, and green color represents the spin-up and
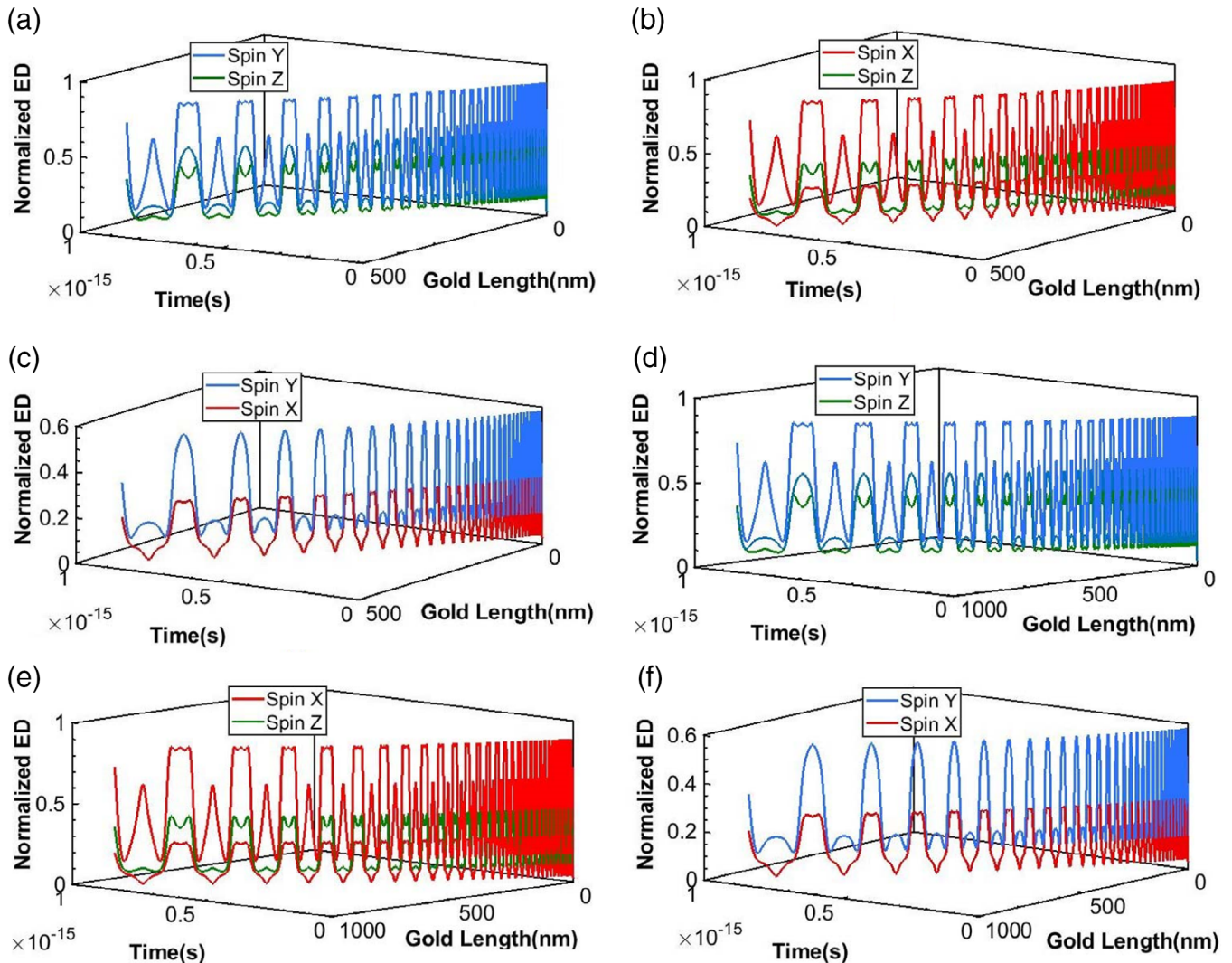

FIGURE 3 Plot of the electron cloud spin projections generated by the electron cloud: (a)–(c) for 500 nm gold length, whereas (d)–(f) for 1,000 nm gold length [Color figure can be viewed at wileyonlinelibrary.com]
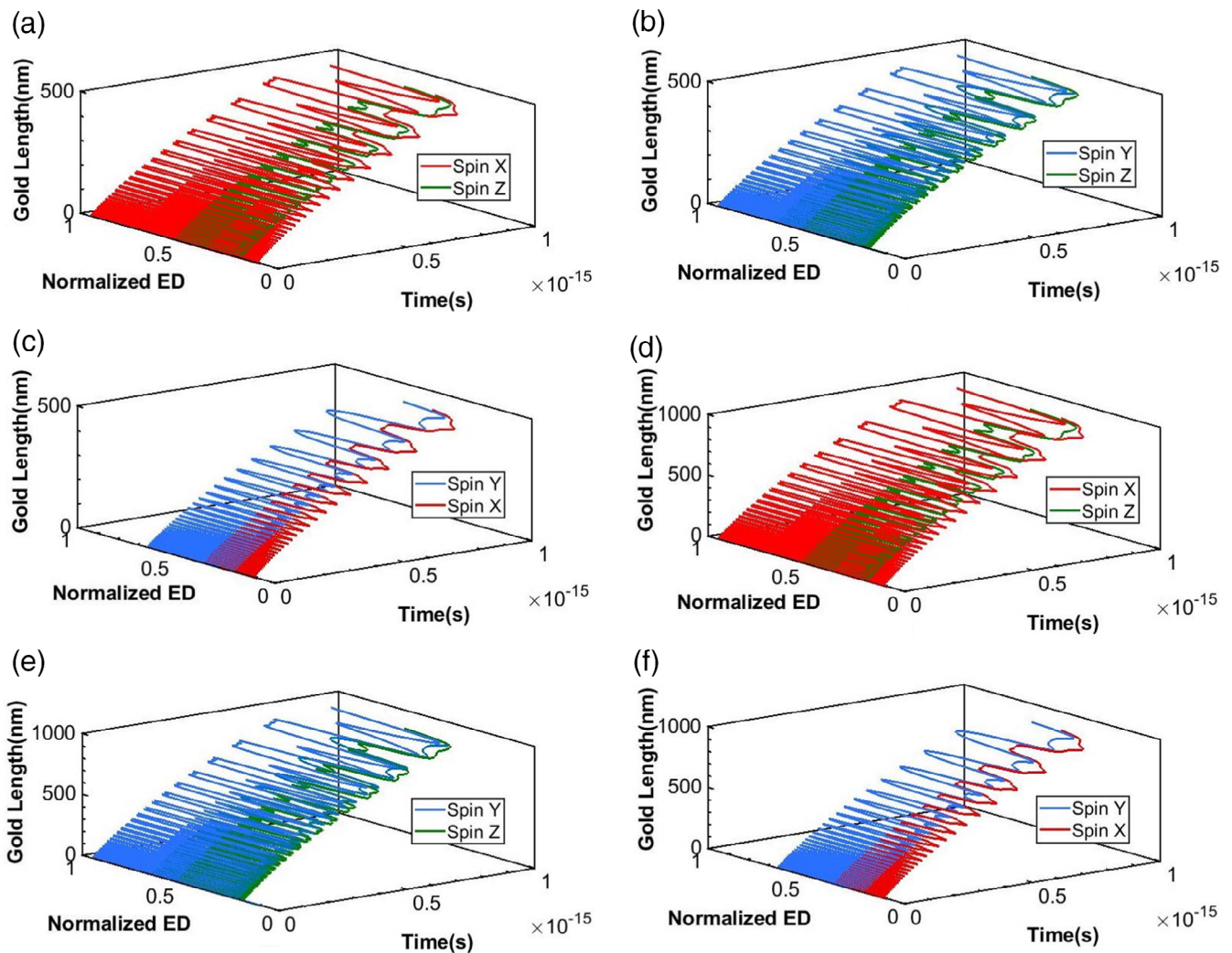
FIGURE 4 Plot of the spin projection into the planes, where (a)–(c) for 500 nm gold length, whereas (d)–(f) for 1,000 nm gold length [Color figure can be viewed at wileyonlinelibrary.com]

spin-down propagating along the z-axis. The obtained slopes for all gold layer lengths are shown the linearity trends as the gold layer length increases. The sensitivity in the x–y direction increases, in the x–z direction is constant, in the y–z direction decreases. The slope values in the x–z direction are constant because the spin numbers and time assumed to be the same. The induced changes in the electron cloud at the center ring by the surrounded environment affected the output interferometer. It measured in terms of the changes of the electron spin with times, from which the ultra-high measurement resolution achieved. In this work, the scanning range of fs obtained.

4 | CONCLUSION

A 3D-quantum interferometer using the electron cloud trapping and transportation within a silicon microring circuit proposed. The interferometer function based on the electron cloud sensor spins

projection control. The changes in the gold layer length at the sensing arm produces changes in the quantum interference that are detected at the recovery arm. Regarding the manipulation, the changes in the gold layer length at the sensing arm produces changes in the quantum interference detected at the recovery arm. The gold grating at the center of the silicon microring forms the plasmonic sensors, where the dipole oscillations from the polaritons induce the trapped electron densities. The trapped electron cloud can transport via wireless and cable connections using the generated antenna and cable connection, respectively. From the obtained results, the sensing sensitivities of the 3D quantum interferometer for three gold layer lengths of 100 nm, 500 nm, and 1,000 nm are (47.62 nm fs^{-1}, ±0.4762 fs^{-1}, ±0.01 nm^{-1}), (238.10 nm fs^{-1}, ±0.4762 fs^{-1}, ±0.002 nm^{-1}), (476.20 nm fs^{-1}, ±0.4762 fs^{-1}, ±0.001 nm^{-1}) in the x–y, x–z, and y–z directions, respectively. The silicon microring circuit can also form the plasmonic antenna, which can apply in quantum computing, quantum communication, and quantum cellular automata based on the spin projections.
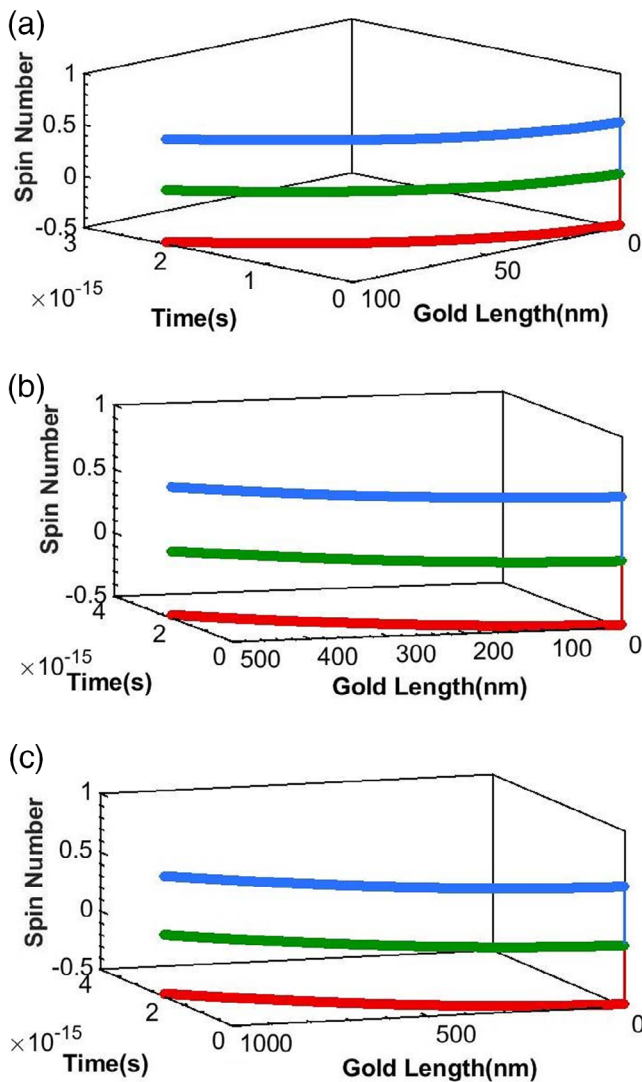
FIGURE 5 Plot of the 3D-quantum interferometer simulation results, where (a)–(c) for 100 nm, 500 nm, and 1,000 nm gold length, respectively [Color figure can be viewed at wileyonlinelibrary.com]
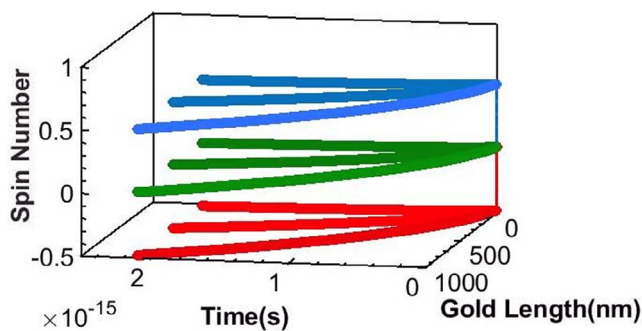

FIGURE 6 Plot of the sensor sensitivity, where all three graphs in Figure 5a–c in one graph: where the slopes are the sensitivities [Color figure can be viewed at wileyonlinelibrary.com]

CONFLICT OF INTEREST

The authors have declared that this work has no conflict of interest.

ORCID

Gaurav Kumar Bharti https://orcid.org/0000-0002-7613-5062
Preecha Yupapin https://orcid.org/0000-0002-6438-9276

REFERENCES

Agrawal, G. P. (2011). Nonlinear fiber optics: Its history and recent progress [invited]. *Journal of Optical Society America B, 28*(12), A1–A10.

Amit, O., Margalit, Y., Dobkowski, O., Zhou, Z., Japha, Y., Zimmermann, M., ... Folman, R. (2019). T³ Stern-Gerlach matter-wave interferometer. *Physical Review Letters, 123,* 083601.

Bass, M., Eric, W. V. S., David, R. W., & William, L. W. (1994). *Handbook of optics* (2nd ed.) (Vol. 2, pp. 21.1–21.28). New York: McGraw-Hill, INC.

Blaber, M. G., Arnold, M. D., & Ford, M. J. (2009). Search for the ideal plasmonic nanoshell: The effects of surface scattering and alternatives to gold and silver. *Journal of Physical Chemistry C, 113,* 3041–3045.

Chen, Y., Fink, M., Steinlechner, F., Torres, J. P., & Ursin, R. (2019). Hong-Ou-Mandel interferometer on a biphoton beat note. *NPJ Quantum Information, 5,* 43.

Filip, K., Benjamin, A. S., Klaus, H., Yaakov, Y. F., Philipp, G., Lukas, M., ... Markus, A. (2019). Concepts for long-baseline high-mass matter-wave interferometer. *Physica Scripta, 94,* 3.

Foreman, M. R., Swaim, J. D., & Vollmer, F. (2015). Whispering gallery mode sensors. *Advances in Optics and Photonics, 7*(2), 168–240.

Khajemiri, Z., Lee, D., Hamidi, S. M., & Kim, D. S. (2019). Rectangular plasmonic interferometer for high sensitive glycerol sensor. *Scientific Reports, 9,* 1378.

Kim, H., Lee, S. M., Kwon, O., & Moon, H. S. (2017). Two-photon interferometer of polarization-entangled photons in a Franson interferometer. *Scientific Reports, 7,* 5772.

Li, D., Feng, J., & Pacifici, D. (2016). Nanoscale optical interferometer with incoherent light. *Scientific Reports, 6,* 20836.

Nadine, D., Jonas, R., Philipp, G., von Issendorff, B., Philipp, H., & Markus, A. (2014). Photofragmentation beam splitters for matter-wave interferometery. *Physical Review Letters, 113,* 233001.

Nagarajan, A., Van Erve, K., & Gerini, G. (2020). Ultra-narrowband polarization insensitive transmission filter using a coupled dielectric-metal metasurface. *Optics Express, 20,* 773–787.

Nandy, A., Biplab, P., & Chakrabarti, A. (2014). Exotic electron states and tunable magneto-transport in a fractal Aharonov–Bohm interferometer. *Physics Letters A, 378,* 3144–3150.

OptiFDTD Technical Background and Tutorials (Finite Difference Time Domain) Photonics Simulation Software, Version 12.0. http://www.optiwave.com, Searched on 20th Sept, 2019.

Pooch, A., Seidling, M., Layer, M., Rembold, A., & Stibor, A. (2017). A compact electron matter wave interferometer for sensor technology. *Applied Physics Letters, 110,* 223108.

Pornsuwancharoen, N., Amiri, I. S., Suhailin, F. H., Aziz, M. S., Ali, J., Singh, G., & Yupapin, P. (2017). Micro-current source generated by a WGM of light within a stacked silicon-graphene-Au waveguide. *IEEE Photonics Technology Letters, 29,* 1768–1771.

Pornsuwancharoen, N., Youplaoa, P., Amiri, I. S., Ali, J., Poznanski, R. R., Chaiwong, K., & Yupapin, P. (2018). On-chip polariton generation using an embedded nanograting microring circuit. *Results in Physics, 10,* 913–916.

Prabhu, A. M., Tsay, A., Han, Z., & Van, V. (2010). Extreme miniaturization of silicon add-drop microring filters for VLSI photonics applications. *IEEE Photonics Journal, 2,* 436–444.

Prateep, P., Surasak, C., & Yupapin, P. (2016). Analytical and simulation of a triple micro whispering gallery mode probe system for a 3D blood flow rate sensor. *Applied Optics*, *55*, 9504–9513.

Prince, G. (2018). Controlling level splitting by strong coupling of surface plasmon resonances with rhodamine-6G on a gold grating. *Plasmonics*, *13*, 2067–2077.

Punthawanunt, S., Aziz, M. S., Phatharacorn, P., Chiangga, S., Ali, J., & Yupapin, P. (2018). Lifi cross-connection node model using whispering gallery mode of light in a microring resonator. *Microsystem Technologies*, *24*, 4833–4838.

Russ, M. & Burkard, G. (2017). Three-electron spin qubits. *Journal of Physics: Condensed Matter 29*, 393001, 1–36.

Spagnolo, N., Aparo, L., Vitelli, C., Crespi, A., Ramponi, R., Osellame, R., ... Sciarrino, F. (2012). Quantum interferometer with three-dimensional geometry. *Scientific Reports*, *2*, 862.

Szuatakowski, M., & Palka, N. (2005). Contrast sensitive fiber optic Michelson interferometer as elongation sensor. *Opto-Electronics Review*, *13*(1), 19–26.

Tamee, K., Srinuanjan, K., Mitatha, S., & Yupapin, P. P. (2011). Distributed sensors using panda ring resonator type in multiwavelength router. *IEEE Sensors*, *11*(9), 1987–1992.

Trong, H. B. N., & Chang, Y. C. (2017). Whispering gallery modes in hybrid AU-ZnO microsphere resonators: Experimental and theoretical investigations. *Optical Materials Express*, *7*(8), 2962–2967.

Tunsiri, S., Thammawongsa, N., Threepak, T., Mitatha, S., & Yupapin, P. (2019). Microring switching control using plasmonic ring resonator circuits for super-channel use. *Plasmonics*, *14*, 1669–1677.

Yang, S., & Zhang, G. (2018). A review of interferometery for geometric measurement. *Measurement Science and Technology*, *29*, 10.

Yupapin, P. P., Pornsuwanchroen, N., & Chaiyasoonthorn, S. (2008). Attosecond pulse generation using nonlinear micro ring resonators. *Microwave and Optical Technology Letters*, *50*, 3108–3111.

Zhang, J., Guo, K., Gao, M., Gao, Y., & Yang, J. (2017). Design of polarization-insensitive high-visibility silicon-on-insulator quantum interferometer. *Scientific Reports*, *8*, 14613 (2018).

Zulicke, U., & Signal, A. I. (2007). Rashba interferometers: Spin-dependent single- and two-electron interference. *Solid State Communications*, *144*, 529–535.